33RD CONGRESS
OF THE INTERNATIONAL COUNCIL
OF THE AERONAUTICAL SCIENCES
STOCKHOLM, SWEDEN, 4-9 SEPTEMBER, 2022

ICAS 2022 SWEDEN

High-accurate Numerical Simulation for Vortex Flow Over a Slender Missile at High Angle of Attack

Chang-Hao Gao[1], Wen-Ping Song[1*], Shao-Qiang Han[1,2], Kuan Lu[1],

Yue Wang[1], Zhong-Hua Han[1], Bin Wu[3,4]

1 Institute of Aerodynamic and Multidisciplinary Design Optimization,
National Key Laboratory of Science and Technology on Aerodynamic Design and Research,
College of Aeronautics, Northwestern Polytechnical University, Xi'an, 710072, P. R. China
2 Tianfu Engineering-oriented Numerical & Software Innovation Center,
College of Computer Science, Sichuan University, Chengdu, 710071, P. R. China
3 Shanghai Electro-mechanical Engineering Institute, Shanghai, 201109, P. R. China
4 College of Astronautics, Nanjing University of Aeronautics and Astronautics, Nanjing, 211106, P. R. China

Abstract

Accurate simulation of asymmetrical vortical flow over slender missiles at high angles of attack is crucial for predicting the aerodynamic characteristics of missiles. However, numerical solution for vortices is very sensitive to numerical dissipation. A novel high-order scheme (WENO-K) proposed by our research group can effectively reduce numerical dissipation and capture vortex structures more accurately compared to classical WENO schemes. In this paper, a new numerical method combining 5th WENO-K and IDDES is developed to accurately solve the supersonic unsteady viscous flow dominated by complex asymmetrical vortices over the Sparrow III type missile, and the mechanism of how asymmetrical vortices affect aerodynamic forces of the missile is revealed.

Keywords: Slender Missile, High-order Scheme, WENO-K, IDDES

1. General Introduction

Strong shock waves and complex vortices are the main characteristics of flow over a maneuvering tactical missile at high angles of attack. As early as the 1950s[1], exploration of the flow characteristics of slender bodies has been carried out. For the slender missile with an apex (slender pointed body), as the angle of attack α exceeds a certain value ($20° \le \alpha \le 70°$)[2], even if the sideslip angle β is zero, the lee side of the missile will develop a series of complex asymmetric vortices. Two asymmetric vortices rise from free shear layers and tears after developing along an axial length, shedding left and right alternately. This process is cyclical in the spatial sense rather than temporal, so-called "steady" asymmetric vortices, which can be associated with Karman Vortex Street. The vortex system induces an asymmetric pressure distribution on the surface of a missile. Integration of the pressure distribution over the surface yields a net side force, along with a yawing and rolling moment. Under some flight conditions, the side force could even reach the magnitude of normal force acting on the body and seriously affect the flight quality of the missile, which is the flow phenomenon addressed in the paper.

Although a lot of research has been carried out, the physical mechanism of asymmetric vortices still lacks in-depth understanding. CFD (Computational Fluid Dynamics) has become an effective method of solving complex flows. Xu et al[3] study the non-linear effect of a tactical missile's rolling moment at a high angle of attack by solving RANS (Reynolds-averaged Navier-Stokes) equations, and the results indicate that RANS with a low-order scheme has the capability of capturing large scale separation vortices. Zhang[4] compared the different results simulated by DES (Detached-Eddy Simulation) and RANS for the asymmetry vortex flow over a slender body, the result shows that DES is more

appropriate for large separation simulation. Wang et al[5]. used DDES (Delayed Detached-Eddy simulation) and oil-flow visualization experiment to study the transient unsteady flow characteristics of a slender body at very large angles of attack ($\alpha=0^\circ \sim 180^\circ$).

However, most existing CFD methods are not adequate for vortex-dominated flows since the vortex structures are very sensitive to numerical dissipation, while low-order methods and lack of grid resolution both involve excessive numerical dissipation.

Conventional low-order schemes perform excessive numerical dissipation, which always weaken the generation of vortices and make it difficult to capture the evolution of vortices. Increasing the size of discretization stencil can decrease numerical dissipation, while unlimitedly increasing discretization order results in excessively growing computational costs. Fifth-order WENO (Weighted Essentially Non-oscillatory) schemes are high-order schemes that balance accuracy and efficiency well. The original WENO scheme was proposed by Liu et al[6]. It is highly favored due to its high precision in both smooth and discontinuous flow regions. Jiang and Shu[7] developed the original WENO scheme (WENO-JS), which is more efficient and robust. WENO-JS scheme is the foundation for the explosive development of WENO schemes, improvements of WENO never stop[8]-[10]. However, these WENO schemes are all based on polynomial interpolations and their convex combination at the cell boundaries. Once the number of cells participating in interpolation stencil is fixed, the accuracy can only achieve the order of polynomial interpolation at most. When the size of the stencil is larger than three cells, the computational cost will significantly increase. Instead of enlarging the stencils, Han[11], the third author of the present paper, proposed a novel WENO scheme (WENO-K) that adopts non-polynomial Gauss functions and Kriging interpolation to improve the order of accuracy for the reconstruction by involving a free hyper-parameter. WENO-K scheme allows the hyper-parameter to be adaptively optimized by using a local solution so that the local accuracy is improved and numerical dissipation can be reduced. At the same time, an effective indicator is constructed to efficiently eliminate the unreasonable hyper-parameters evaluated on troubled cells that contain discontinuities. WENO-K scheme can be easily applied to any improved variants of WENO schemes to enhance their accuracy in smooth regions. This scheme has been successfully implemented in the flow simulation for rotors in hover[12], effectively preserving vortex wake to a larger wake age with a more accurate trajectory of vortex core, and capturing more sophisticated unsteady vortex structures with higher resolution for discontinuities than WENO-JS scheme with a little increase in computational cost.

Accurate vortex flow simulation depends not only on the high-order scheme but also on the ability of physical model to simulate complex turbulent flow. The Reynolds number of real aircraft can reach a large magnitude of 10^7~10^9, and flow around the aircraft is dominated by turbulence. Therefore, the accuracy of massive separation simulation is highly related to the turbulence model. Unsteady RANS can only capture large-scale vortices while there are a large number of small-scale vortex structures in the physical flow. To further study the mechanism of asymmetric vortices, the high-order and low dissipation numerical scheme and advanced turbulence models should be involved altogether. The hybrid RANS/LES methods are comprehensive choices that balance accuracy and efficiency [13]. Among existing hybrid RANS/LES methods, DES methods are relatively complete and widely used. The basic idea of DES[14] is to combine LES (Large-Eddy Simulation) and RANS according to the characteristics of large-scale and small-scale pulsation, RANS is adopted in dissipation-dominated regions while LES is adopted in large-eddy transport dominated regions. Original DES relies heavily on the grid distribution[15], which has been improved by DDES[17] and IDDES[16] (Improved Delayed Detached-Eddy Simulation). In this paper, a novel numerical method combining WENO-K scheme and IDDES is developed to accurately solve the vortex-dominated flow over missiles.

Existing studies mainly focus on the revolutionary slender body, for tactical missiles, there exists lifting surfaces (wings), control surfaces (rudders), and other components, which further complicate the flow. The numerical method proposed in this paper is applied to the supersonic unsteady viscous flow dominated by complex vortices over the Sparrow III type missile and the mechanism of asymmetrical vortices will be revealed.

The rest of this paper is organized as follows: In Section 2, the numerical method including WENO-K scheme and IDDES is described. Validation of the numerical method is presented in Section 3. In Section 4, a simulation of vortical flow over the missile is conducted and results are discussed. Finally, we give a brief conclusion in Section 5.

2. Methodology

2.1 Governing equations

The numerical simulation in this paper adopts an in-house CFD flow solver. The flow governing equations are discretized under the framework of finite-difference method. The flow solver can solve 2D/3D, incompressible/compressible, steady/unsteady, Euler/NS equations. It integrates a variety of spatial discretization schemes including fifth-order WENO-K schemes, time-marching schemes, and turbulence models that can be run as hybrid RANS/LES models.

Viscosity should be taken into account in accurate numerical simulation. Therefore, the NS equation is adopted as flow governing equation. In the generalized coordinates, the 3D unsteady NS equations under the framework of finite-difference method may be written as

$$\frac{\partial \hat{q}}{\partial t}+\frac{\partial \hat{E}}{\partial \xi}+\frac{\partial \hat{F}}{\partial \eta}+\frac{\partial \hat{G}}{\partial \zeta}=\frac{\partial \hat{E}_v}{\partial \xi}+\frac{\partial \hat{F}_v}{\partial \eta}+\frac{\partial \hat{G}_v}{\partial \zeta} \tag{1}$$

where $\hat{q}$ is the vector of conserved variables. $\hat{E}$、$\hat{F}$、$\hat{G}$ are convective flux terms, which can be discretized by fifth-order WENO schemes constructed by upwind schemes for accurate calculation, and $\hat{E}_v$、$\hat{F}_v$、$\hat{G}_v$ are viscous flux terms that are discretized by central difference scheme.

SA one-equation model is used for turbulence enclosure and constructing DES class hybrid RANS/LES method. A full implicit dual-time stepping method with SSOR sub-iteration is adopted to advance the unsteady solution of the vortical flow in time. Local time-stepping is applied to accelerate the convergence of sub-iterations.

2.2 WENO-K scheme for spatial discretization

Typical WENO schemes still suffer excessive dissipation in smooth regions. WENO-K[11] scheme utilizes non-polynomial Gauss-kriging reconstructions with a locally adaptive hyper-parameter, while WENO-JS scheme and many of its variants use globally definitive polynomial reconstructions. WENO-K can be easily implemented under the framework of WENO-JS.

Reconstructions of primitive variables $\boldsymbol{Q}=[\rho,u,v,w,p]^T$ are conducted by using fifth-order WENO-JS and WENO-K respectively.

Assume $q_{L,i+1/2}$ is a scalar component of $Q_{L,i+1/2}$, the fifth-order WENO-K interpolation is given by:

$$q_{L,i+1/2}=\omega_0 q_{i+1/2}^{(0)}+\omega_1 q_{i+1/2}^{(1)}+\omega_2 q_{i+1/2}^{(2)} \tag{2}$$

where $\omega_k q_{i+1/2}^{(k)}$ for $k=0,1,2$ are the extrapolated values obtained from cell averages $\overline{q}$ in the k^{th} forth-order (only third-order for WENO-JS) sub stencil $S_k=(i-k,i-k+1,i-k+2)$ and are given by:

$$\begin{cases} q_{i+1/2}^{(0)}=(\frac{1}{3}-\frac{1}{4}\theta)\overline{q}_{i-2}+(-\frac{7}{6}+3\theta)\overline{q}_{i-1}+(\frac{11}{6}-\frac{11}{4}\theta)\overline{q}_i \\ q_{i+1/2}^{(1)}=(-\frac{1}{6}-\frac{1}{4}\theta)\overline{q}_{i-1}+(\frac{5}{6}-\frac{1}{3}\theta)\overline{q}_i+(\frac{1}{3}+\frac{7}{12}\theta)\overline{q}_{i+1} \\ q_{i+1/2}^{(2)}=(\frac{1}{3}+\frac{7}{12}\theta)\overline{q}_i+(\frac{5}{6}-\frac{1}{3}\theta)\overline{q}_{i+1}+(-\frac{1}{6}-\frac{1}{4}\theta)\overline{q}_{i+2} \end{cases} \tag{3}$$

where the interpolation coefficients containing θ is a simplification for results of Gauss-Kriging interpolation, and θ is the hyper-parameter involved by Gauss basis function, which needs to be optimized to enhance the accuracy of reconstruction. After a series of complex error analyses, the optimized hyper-parameter θ can be expressed as

$$\theta=\frac{6}{5}\frac{\overline{q}_{i-1}-3\overline{q}_i+3\overline{q}_{i+1}-\overline{q}_{i+2}}{\overline{q}_{i-1}-15\overline{q}_i+15\overline{q}_{i+1}-\overline{q}_{i+2}} \tag{4}$$

It is obvious that the WENO-K scheme degenerates to WENO-JS scheme when the value of θ equals zero.

Three three-cell stencils are combined with nonlinear weights ω_k $(k=0,1,2)$ to form an interpolation with higher than fifth order. The expressions of nonlinear weights ω_k are given by

$$\omega_k = \frac{\alpha_k}{\alpha_0 + \alpha_1 + \alpha_2}$$
$$\alpha_k = \frac{C_k}{\varepsilon + \mathrm{IS}_k} \tag{5}$$

Where $C_0 = 0.1, C_1 = 0.6, C_2 = 0.3, \varepsilon = 1\times10^{-6}$. IS_k are the "smoothness indicators" of the stencil S_k which are the same as that of the WENO-JS scheme.

The right value $q_{R,i+1/2}$ can be obtained by symmetry of the left and right states. After cartesian coordinate system (x, y, z) is transformed to generalized coordinate system (ξ, η, ζ), spatial dimensions can be approximately decoupled and the reconstruction can be performed very efficiently dimension by dimension.

Table 1[11] shows the reconstruction precision of the fifth-order WENO-K scheme, which can achieve fourth-order while the traditional fifth-order WENO-JS scheme can only achieve third-order under the same sub-stencil. For strict theoretical derivation, see Ref.[11].

Table 1 Error analysis of Gauss-kriging reconstructions on there-cell stencils.[11]

Stencil	Errors of reconstruction
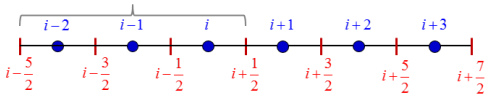	$\left(-\frac{9}{40}\frac{v''_{i+\frac{1}{2}}v'''_{i+\frac{1}{2}}}{v'_{i+\frac{1}{2}}}+\frac{3}{10}v^{(4)}_{i+\frac{1}{2}}\right)\Delta x^4+O\left(\Delta x^5\right)$
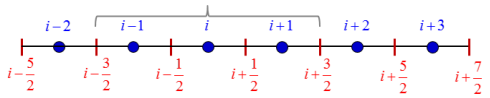	$\left(\frac{1}{40}\frac{v''_{i+\frac{1}{2}}v'''_{i+\frac{1}{2}}}{v'_{i+\frac{1}{2}}}-\frac{1}{30}v^{(4)}_{i+\frac{1}{2}}\right)\Delta x^4+O\left(\Delta x^5\right)$
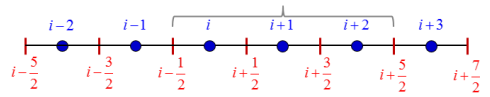	$\left(\frac{1}{40}\frac{v''_{i+\frac{1}{2}}v'''_{i+\frac{1}{2}}}{v'_{i+\frac{1}{2}}}-\frac{1}{30}v^{(4)}_{i+\frac{1}{2}}\right)\Delta x^4+O\left(\Delta x^5\right)$
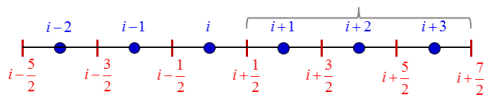	$\left(-\frac{9}{40}\frac{v''_{i+\frac{1}{2}}v'''_{i+\frac{1}{2}}}{v'_{i+\frac{1}{2}}}+\frac{3}{10}v^{(4)}_{i+\frac{1}{2}}\right)\Delta x^4+O\left(\Delta x^5\right)$

2.3 IDDES based on SA one-equation model

IDDES[16] is a kind of DES model which combines DDES[17] with WMLES[18] (Wall Modelling Large-Eddy Simulation).SA-IDDES is constructed by defining a new hybrid turbulence length-scale L_{IDDES}, which is composed of RANS length-scale L_{RANS} and LES length-scale L_{LES}. L_{IDDES} is given by

$$L_{IDDES} = f_{hyb}\left(1+f_{restore}\right)L_{RANS} + \left(1-f_{hyb}\right)L_{LES} \tag{6}$$

For SA-RANS turbulence model, the length-scale L_{RANS} is equal to the distance to the wall

$$L_{RANS} = d_w \tag{7}$$

L_{LES} is defined via the subgrid length-scale Δ as

$$L_{LES} = C_{DES}\Psi\Delta \tag{8}$$

C_{DES} is the fundamental empirical constant of DES[20] and Ψ is a low-Reynolds number correction[17] introduced in order to compensate the activation of the low-Reynolds number terms of some background RANS model in LES mode. Both C_{DES} and Ψ depend on the background RANS model,

and Ψ is equal to 1 if the RANS model does not include any low-Reynolds number terms. For SA-RANS turbulence model

$$C_{DES} = 0.65$$

$$\Psi^2 = \min\left[10^2, \frac{1-\frac{c_{b1}}{c_{w1}\kappa^2 f_w^*}\left[f_{t2}+\left(1-f_{t2}\right)f_{v2}\right]}{f_{v1}\max\left(10^{-10},1-f_{t2}\right)}\right] \tag{9}$$

Where all the notations, except for the quantity $f_w^* = 0.424$, are the same as in the SA-RANS model[19].

In IDDES method, the subgrid length-scale Δ is redefined as

$$\Delta = \min\left\{\max\left[C_w d_w, C_w h_{\max}, h_{wn}\right], h_{\max}\right\} \tag{10}$$

Where h_{wn} is the local grid scale of grid cells in the normal direction of walls. C_w is a constant, usually equals to 0.15. $h_{\max}$ is the maximum length in three directions of grid cells. The definition of Δ includes not only the local grid scale but also the influence of wall distance.

f_{hyb} is the hybrid function that has two branches, DDES branch and WMLES branch

$$f_{hyb} = \max\left\{\left(1-f_{dt}\right), f_{step}\right\} \tag{11}$$

f_{dt} is the delaying function defined in DDES method

$$f_{dt} = 1-\tanh\left(\left[8r_{dt}\right]^3\right) \tag{12}$$

The quantity r_{dt} is borrowed from SA-RANS turbulence model[19]

$$r_{dt} = \frac{\mu_T}{\kappa^2 d_w^2 \sqrt{0.5\left(|S|^2+|\Omega|^2\right)}} \tag{13}$$

Where $|S|$ represents the modulus of the strain rate tensor, $|\Omega|$ represents the modulus of the rotation rate tensor (vorticity).

f_{step} only works when the WMLES model is activated, it makes RANS to quickly convert to LES in the boundary layer. It can be structured as:

$$f_{step} = \min\left\{2\exp(-9\alpha)^2, 1.0\right\} \tag{14}$$

Where $\alpha = 0.25 - d_w / h_{\max}$. The value of f_{step} ranges from 0 to 1, When $0.5h_{\max} < d_w < h_{\max}$, it can transform RANS mode ($f_{step} = 1.0$) to LES mode ($f_{step} = 0.0$) quickly.

3. Validation

3.1. Sparrow III type missile at Ma=1.5

The AIM-7 “Sparrow” missile is a slender revolutionary body with a coned apex, four trapezoidal wings and four triangular fins arranged in a normal configuration as "++" layout. The missile has detailed wind tunnel test data[21], which is chosen to validate the flow solver and the high-accurate numerical simulation method proposed in this paper.

The numerical simulation is performed at the following conditions

$$Ma = 1.5, \dot{\mathrm{R}}\mathrm{e} = 8.2\times10^6 / m, \alpha = 0 \sim 45°, \gamma = 0°.$$

Figure 1 presents the multi-block overset structured grid system used to discretize computational domain, which is composed of an off-body Cartesian background grid block and 19 near-body grid blocks. The far-field boundary is about $50l$ where l is the length of missile, we take strict control of the cell height in the first layer $(y^+ < 1)$. The number of off-body gird points is about 27 million and the number of near-body gird points is about 23 million, the total number of grid points is about 50 million.

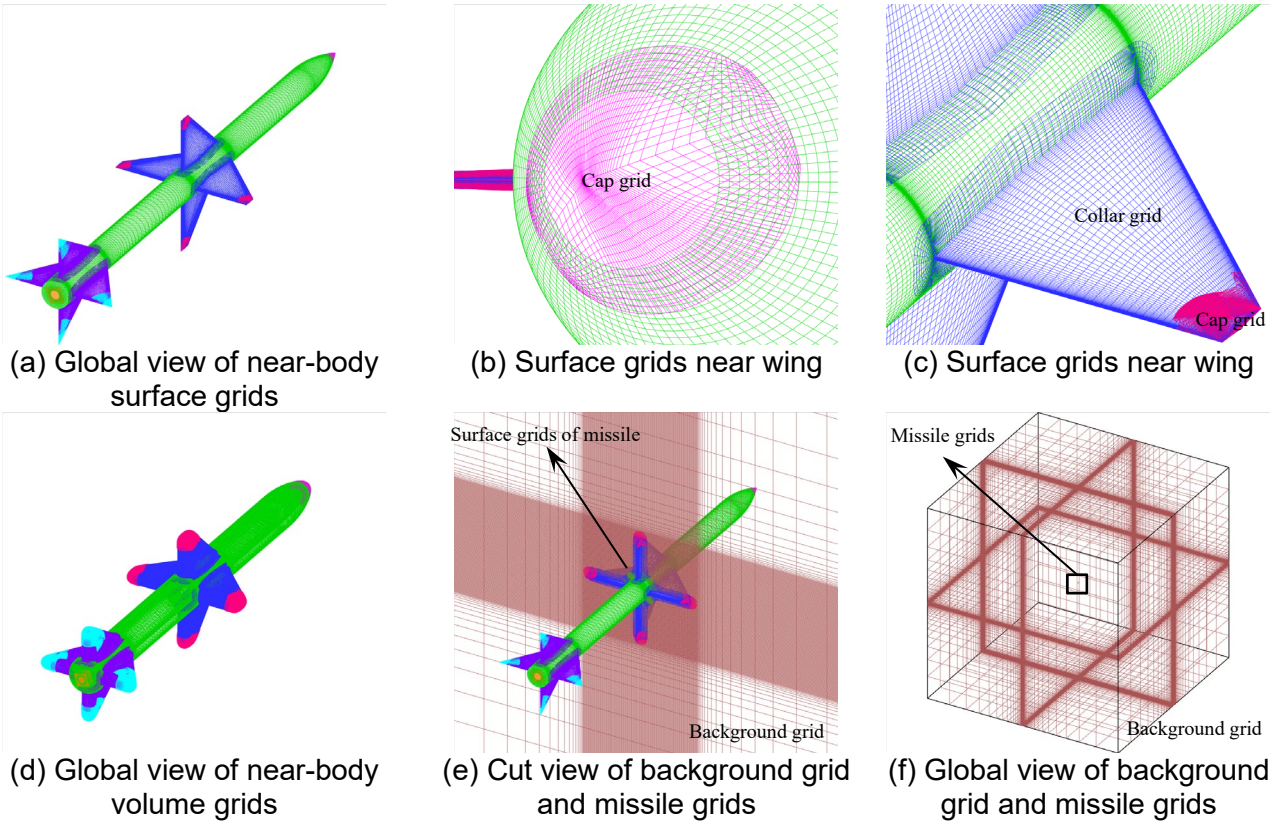

(a) Global view of near-body surface grids (b) Surface grids near wing (c) Surface grids near wing

(d) Global view of near-body volume grids (e) Cut view of background grid and missile grids (f) Global view of background grid and missile grids

Figure 1 Computational grid system for Sparrow III type missile.

5th WENO-K based on Roe upwind scheme is employed to discretized the convective term of RANS equation. The comparison of computed pitch-control characteristics and experimental data is shown in Figure 2. It can be seen that the computed normal C_N, C_L, C_A are in good agreement with the experimental data at different α, while C_A and C_M shows a little discrepancy with the experiment data. The results of computed aerodynamic force/moment coefficient prove that the quality and quantity of the overset grid system adopted are sufficient, which will be used in subsequent section.

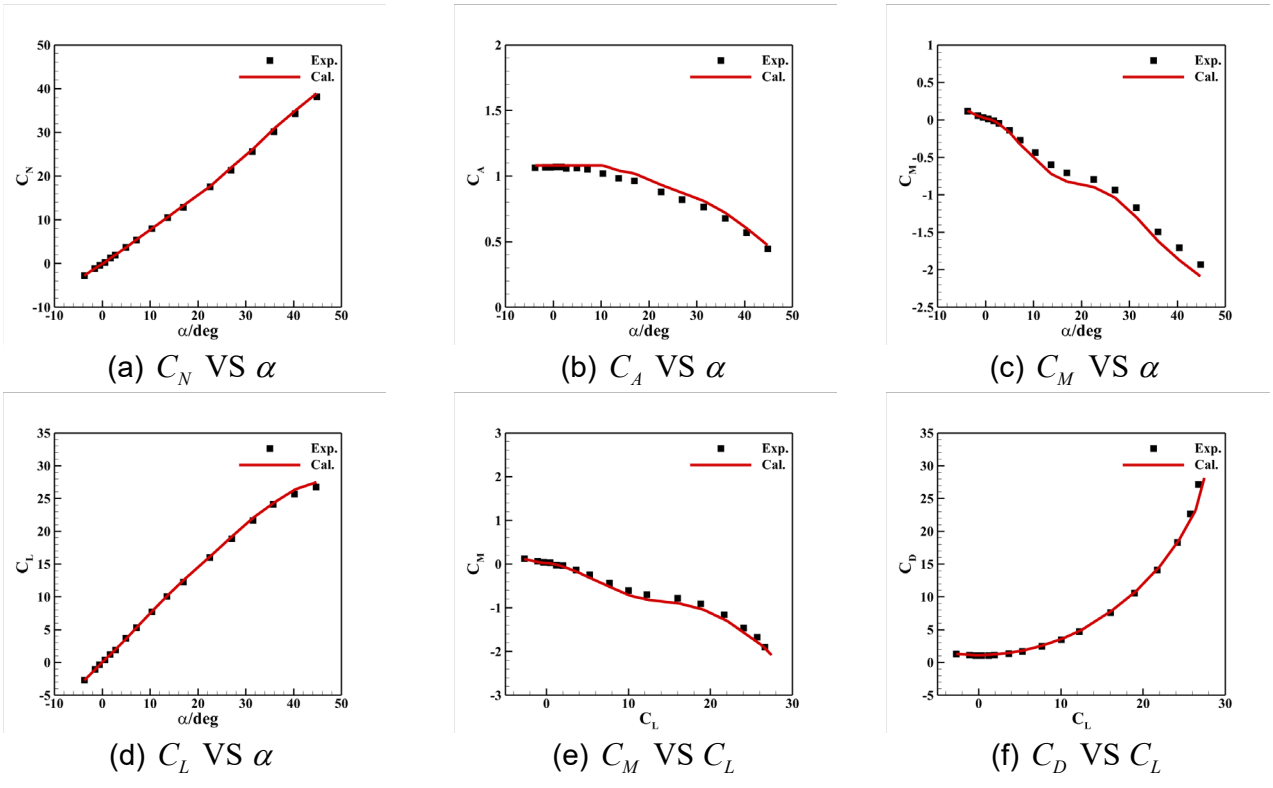

(a) C_N VS α (b) C_A VS α (c) C_M VS α

(d) C_L VS α (e) C_M VS C_L (f) C_D VS C_L

Figure 2 Pitch-control characteristics of Sparrow III type missile at $Ma = 1.5$.

3.2. NACA0021 at α of 60°

The deep stall of airfoil is a kind of typical complex flow with massive separation, which is difficult to be simulated by RANS method. Swalwell et al[22] provided a wealth of wind tunnel test data for NACA0021 at large angles of attack, which has been listed as one of the standard cases by DESider[23] (Detached Eddy Simulation for Industrial Aerodynamics). It is used to validate the capability of accurate numerical method combing WENO-K scheme and SA-IDDES used in this paper.

The flow condition of numerical simulation is

$$Ma = 0.1, \mathrm{Re}_c = 2.7\times10^5, \alpha = 60°$$

Figure 3 presents the two-dimensional grid of NACA0021, it is an O-type grid in the xOz plane. The far-field boundary is about $100c$, where c is the chord length of airfoil. There are 289 and 289 nodes in the circumferential and normal directions, minimum wall distance is 5×10^{-5}c. Referring to the study on the influence of spanwise length in DESider[23], the spanwise length is set as 4c and 161 points are distributed with an equal space of 0.025c. Symmetry with no reflection boundary condition is applied in the spanwise direction.

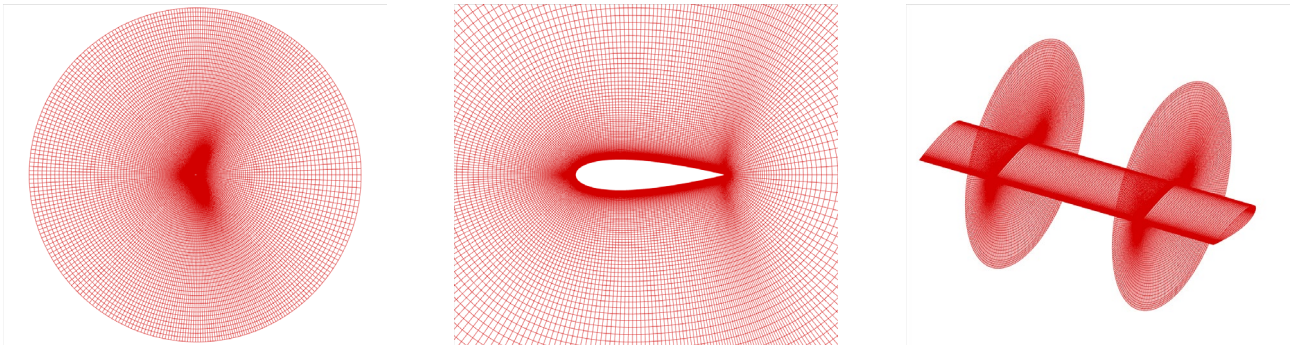

(a) Global view of the grid (b) Grid around the foil (b) Cut view of O grid for airfoil

Figure 3 Computational grid system for NACA0021 airfoil.

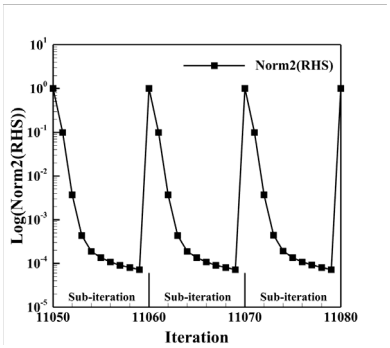

Figure 4 History of residual

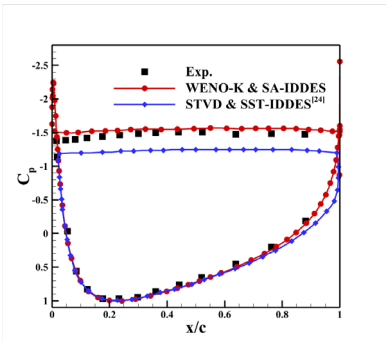

Figure 5 Comparison of mean pressure coefficients

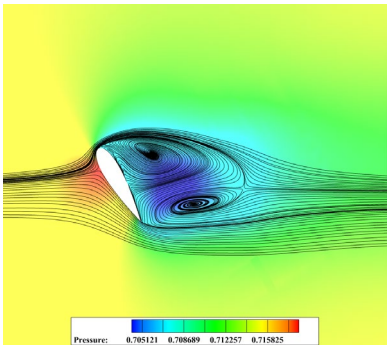

Figure 6 Time-averaged vortex structures

Because the grid system is simple and the node distribution is relatively uniform, low-Reynolds number correction is not activated in calculation The physical time step is $0.01c/U_\infty$, with 10 sub-iterations for each time step, which gives at least a third-order sub-iteration drop between time steps. Figure 4 shows the residual history of simulation, the norm of residual can drop four orders of magnitude in a physical time step, reaching a good convergence. The comparison of time-averaged pressure coefficients C_p distribution is shown in Figure 5, it can be seen that the upper surface of airfoil is almost fully separated. Compared with the calculated results in Ref.[24], which adopts a high-order STVD (Symmetric Total Variation Diminishing) scheme based on Roe scheme that combines a 6th order symmetric scheme and a 5th order WENO scheme (S6WENO5) with adaptive dissipation and SST-IDDES, the numerical result in this paper is in better agreement with experiment. The computed C_p distribution on the lower surface is almost identical with experimental data while the reference result is deviated from experiment near tailing edge. The C_p distribution on the upper surface is more consistent with experiment than reference result. Figure 6 shows the time-averaged C_p contours and streamlines of the airfoil, the upper surface of airfoil is a completely low-pressure

area, while the lower surface has a certain high-pressure area, two large vortices sheds away from the leading and trailing edge respectively. Figure 5 proves that the numerical method developed in this paper shows higher accuracy and lower numerical dissipation characteristic than existing high-accurate numerical simulation.

4. Results and discussion

The flow field of Sparrow III type missile at $\alpha = 40°$ was simulated by using the flow solver and highly accurate numerical method introduced in Section 2. The computational case adopts the same grid system with the validation case in Section 3.1. All simulations are carried out on Sugon supercomputing system of CAS (Chinese Academy of Sciences) in Xi'an. Each computing node is configured by two HYGON2 CPUs (x86 7285 @ 2.00 GHz) with 32 cores, namely, 64 processors per node. The HYGON series of high-performance processors are independently developed by CAS and have been widely used in the industrial field.

256 processors (255 sub-processors and 1 main processor) are used and the grid load of each sub-processor is about 200 thousand, which strictly conforms to the load balance between processors and can maximize the efficiency of parallel computing.

The flow condition of numerical simulation is

$$Ma = 1.5, \dot{\mathrm{R}}\mathrm{e} = 8.2 \times 10^6 / m, \alpha = 40°$$

The physical time step is $0.001D / U_\infty$, where D is the maximum body diameter of the missile, with 20 sub-iterations for each time step. IDDES is restarted on flow field that is initialized by 100 thousand iterations of URANS. Table 2 shows errors of aerodynamic force/moment coefficients between computations and experiment where IDDES result has been time-averaged, URANS results agree well with the experimental data while IDDES can further improve the accuracy of aerodynamic force (moment). The high-accuracy prediction of aerodynamic characteristics is not the only advantage of the numerical method proposed in this paper.

Table 2 Comparison of pitch-control characteristics between computation and experiment.

Method	C_A (Error (%))	C_N (Error (%))	C_M (Error (%))
Experiment	0.57955	33.894	-1.6852
URANS+5th WENO-K	0.59983(3.5)	34.707(2.4)	-1.8083(7.3)
IDDES+5th WENO-K	0.59636(2.9)	34.607(2.1)	-1.7982(6.7)

Figure 7 shows the comparison of vorticity contours calculated by URANS and IDDES on different cutting planes that is perpendicular to the body axis. Figure 7(a) shows the general view of different cutting planes along the axis, where x / D represents the axial position, and $x / D = 0$ is the apex of the missile. It can be seen from Figure 7(b), (c) that the vortex structures calculated by IDDES is much more complex than RANS. Vorticity pattern simulated by URANS on the first several planes near the apex is similar to IDDES. After the vortices evolve along the axis, vortices lifted off and shed away, RANS can no longer capture the shape of vortices well due to the excessive dissipation and time-averaged approximation of turbulence model while IDDES can capture a large number of sophisticated vortices. Although the improvement of accuracy for aerodynamic characteristics is not that significant, IDDES is necessary to study the mechanism of complex vortical flow over the missile.

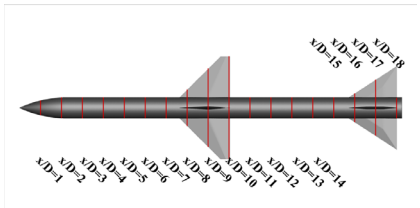

(a) General view of different cutting planes along the axis.

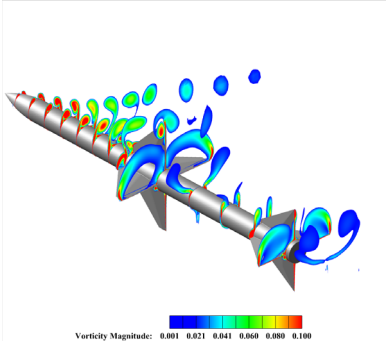

(b) URANS

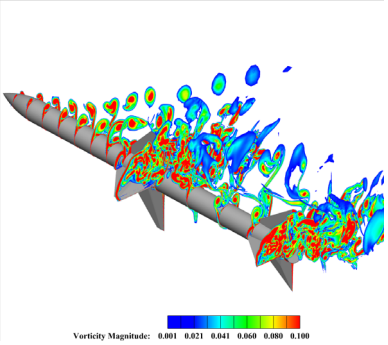

(c) IDDES

Figure 7 Comparison of vorticity contours on different cutting planes along the axis.

Figure 8 shows the variation of vorticity magnitude passing through the vortex cores along the horizontal direction (Y direction) on several cross sections. As we can see, at the first several planes ($x/D=1,2,3$) near the apex, even though the vorticity patterns simulated by RANS and IDDES are basically the same, the vortices calculated by IDDES is stronger than that simulated by RANS. As the asymmetrical vortices travel along the axis, lifting off and shedding away, the vorticity patterns ($x/D=4,5,6$) simulated by RANS is no longer the same as that simulated by IDDES, RANS can only capture the rough shape of shedding vortices, while IDDES results are more complex and can identify the rotation of vortices more clearly. Meanwhile, the vorticity magnitude of vortex cores calculated by IDDES is much higher and the diameter of vortex cores is smaller than that calculated by RANS. It indicates that the numerical dissipation of IDDES is smaller than RANS, and the numerical method proposed in this paper can significantly reduce the non-physical dissipation on vortices.

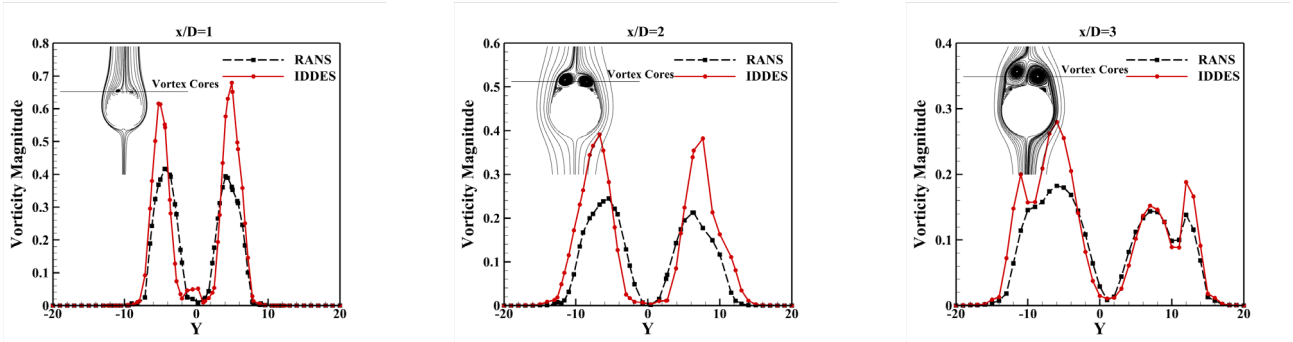

(a) $x/D=1$ (b) $x/D=2$ (c) $x/D=3$

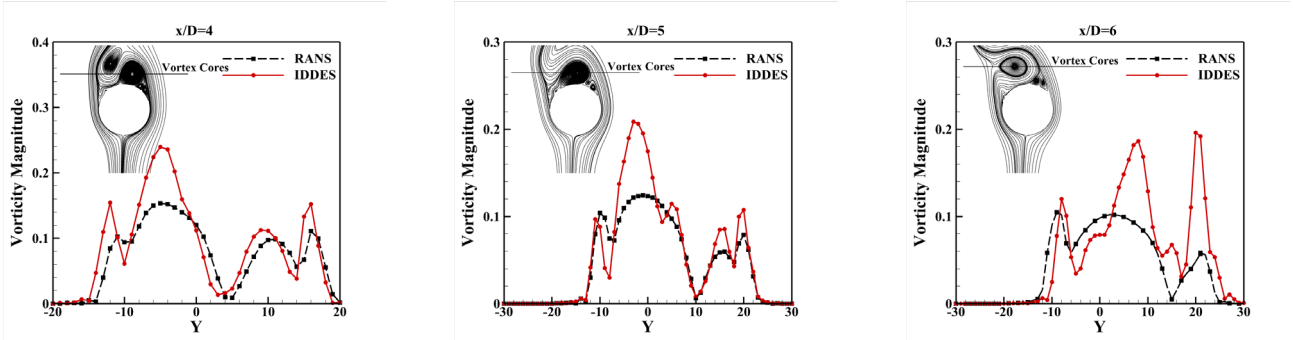

(a) $x/D=4$ (b) $x/D=5$ (c) $x/D=6$

Figure 8 Variation of vorticity magnitude near vortex cores on different cutting planes along the axis.

The aerodynamic interference between components induces new vortex structures and breaks the asymmetric vortices into a series of small-scale vortices, making the vortex-dominated flow around the missile become much more complicated than a single slender revolutionary body. By comparing the vorticity contours simulated by RANS and IDDES in Figure 7, we can see that IDDES can simulate the series of tiny vortex structures above wings and fins, and it can present a stable multi-scale vortex structure on the slender body between wings and fins. However, RANS only roughly simulate the wing tip vortices and the shear layer on the body between wings and fins, and most of small-scale vortices cannot be captured.

The vorticity evolution of RANS and IDDES indicates that even if the higher-order scheme is employed to reduce the numerical dissipation, the complex vortex structures of missile at a high angle of attack still cannot be well captured due to the excessively dissipative and the time-averaged approximation of turbulence model. It is necessary to develop high-accurate numerical methods combining higher accurate physical model and high-order scheme to carry out intensive study on the series of complex flow including the vortex-dominated flow addressed in this paper, which will further deepen people's understanding of complex flow mechanism. In the following part, the flow mechanism of complex vortices of Sparrow missile at high angle of attack will be preliminarily revealed based on IDDES results.

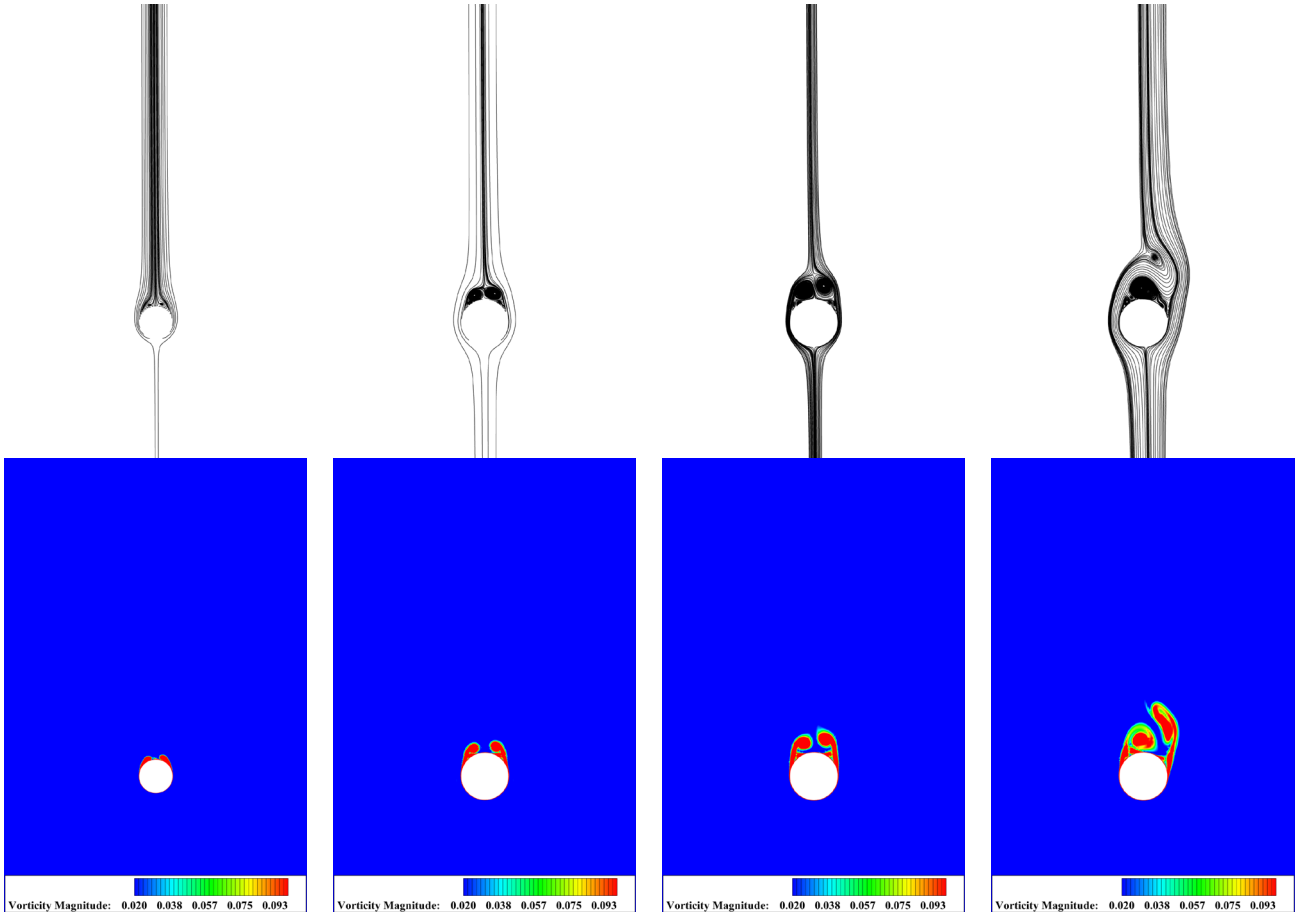

(a) $x/D=1$ (b) $x/D=2$ (c) $x/D=3$ (d) $x/D=5$

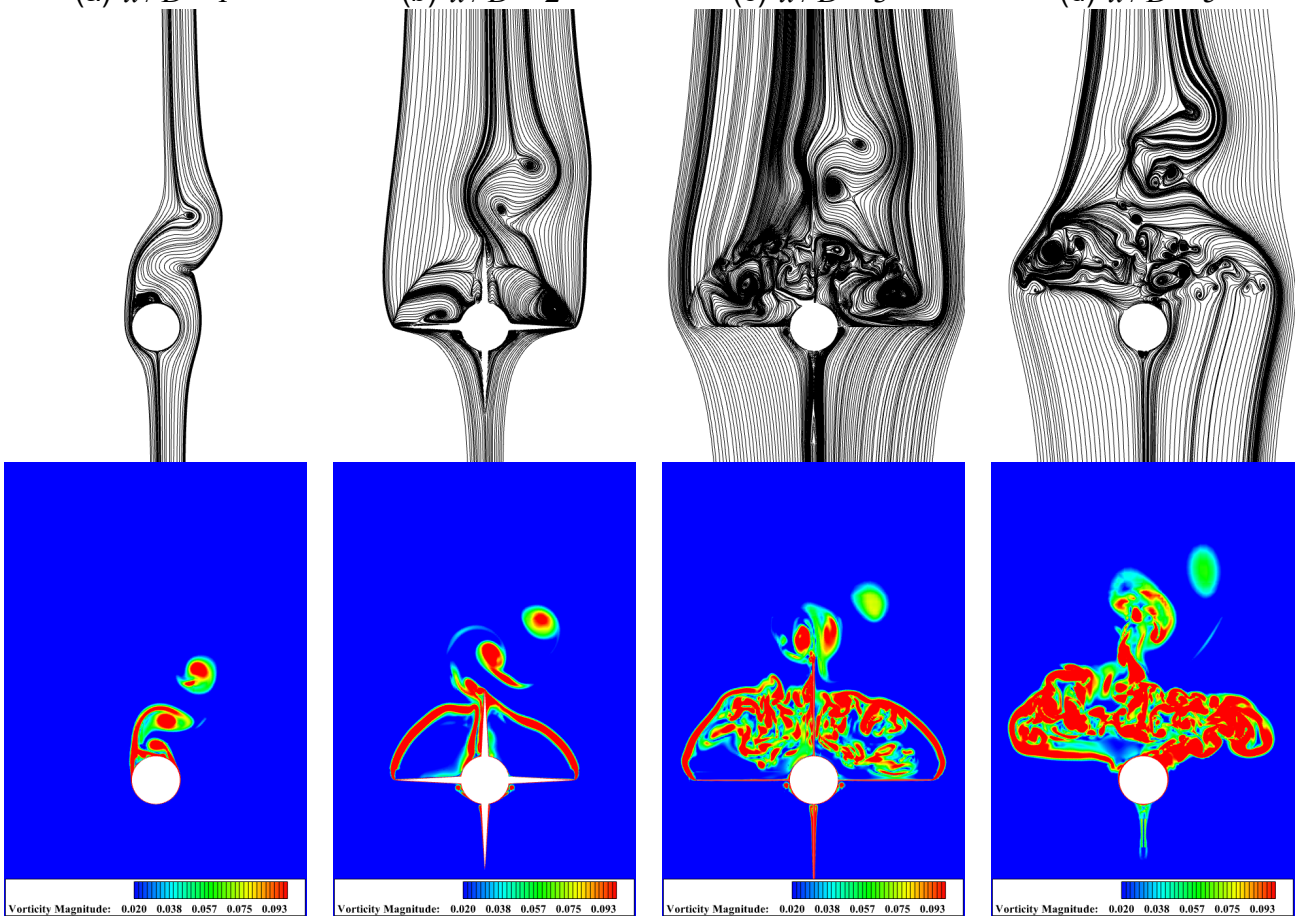

(e) $x/D=7$ (f) $x/D=9$ (g) $x/D=10$ (h) $x/D=11$

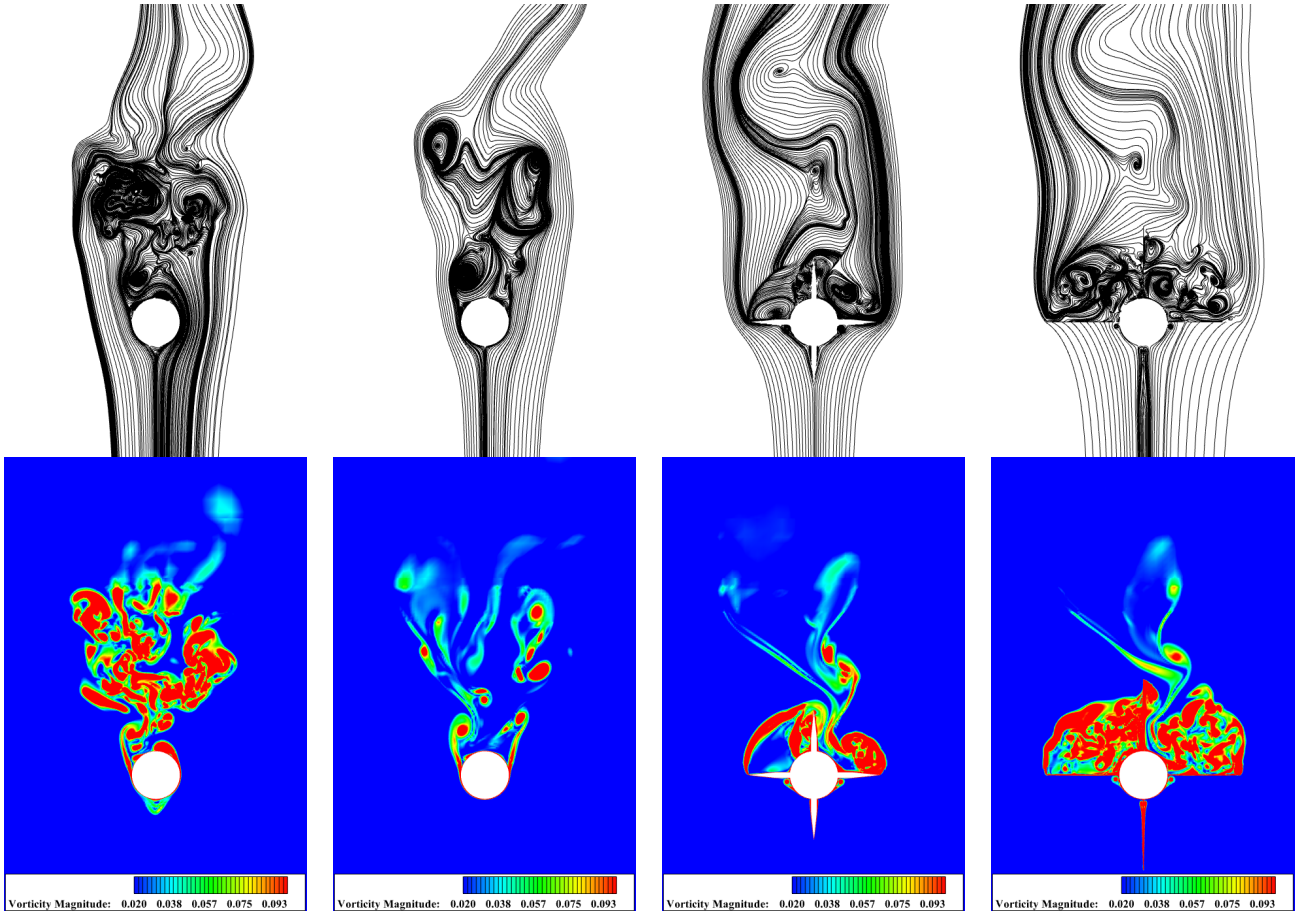

(i) $x/D=13$ (j) $x/D=15$ (k) $x/D=17$ (l) $x/D=18$

Figure 9 Evolution of vorticity contours and streamlines on different cutting planes.

Figure 9 shows the evolution of vorticity contours and streamlines on different cutting planes, it's illustrated that the complexity of vortices structure become more and more complex along the axis. As shown in Figure 9(a), near the apex of the missile, the boundary layer of the lee side separates and rises two asymmetric vortices. There are two different views on the generation mechanism of asymmetry vortices[25], one view holds that the asymmetry is caused by the asymmetry of the boundary layer transition points and separation points on both sides of the configuration, the other holds that the asymmetry is caused by a spatial type of flow instability. It has been proved that the vortex-dominated flow is very sensitive to the disturbance of the apex[25], a small unavoidable geometric imperfection on the apex will lead to significant asymmetric vortices. In numerical simulation, the geometric curvature of the apex could not be strictly satisfied due to the limitation in grid resolution, which will cause a spatial type of flow instability.

As shown in Figure 9(b), the two asymmetric vortices develop downstream along the axis, the separation zone expands in both normal and spanwise directions, forming two strong primary separation vortices. The vorticity generated by the shear layer induces secondary separation in both sides. Figure 10 shows the limiting streamline on the surface of missile, and Figure 10(a) shows the limiting streamlines near the apex. The separation line and reattachment line can be clearly identified. The primary separation point is very close to the apex while the primary separation line is very close to the windward side. The first several cutting planes ($x/D=1,2,3$) in Figure 9(a), (b), (c) show that the primary separation vortices near the apex lifts only a small height in the normal direction, and its spatial direction can basically keep parallel to the axis of the missile.

Figure 9(c) indicates that the right vortex lifts off and sheds away first, since the right secondary vortex and the left primary vortex rotate in the same direction, the two vortices gradually merge into a new primary vortex and then shed away. The two secondary vortices on the left merge into a new primary vortex as well, and then grows stronger along the axis but does not lift off from the wall. The flow on the lee-side of body in front of wings eventually develops into an asymmetric three-vortex structure, then evolves into a more complex flow structure due to aerodynamic interference of wings.

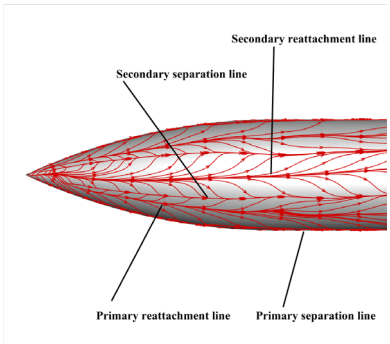

(a) Limiting streamlines pattern near the apex.

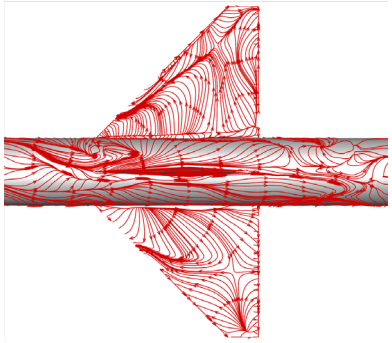

(b) Limiting streamlines pattern of wings.

(b) Global views of limiting streamline of surface.

Figure 10 Limiting streamline

The vortical flow becomes very complicated due to components interference, the shear layer of body is disturbed by wings, and the asymmetric vortices near wall are broken into a series of small-scale vortices. At the same time, new vortex structures are induced by wings, which further complexity of the flow field. Figure 10(b) shows the limiting streamlines near the wings, combined with Figure 9(f), (g), (h), it indicates that leading edge and tip of upper surface of wings rise new vortices, and the separation pattern on the left and right wing is asymmetrical. The lower surface of wing root form a wake region on both sides. At the same time, due to the interference of vertical wing, the separation pattern on the body also becomes very complicated. There appears tertiary separation, and separation lines and reattachment lines are no longer parallel with the axis of missile. The flow pattern near the tail is similar to that of wings.

The lee-side between wings and tails is filled with complex vortex structures downstream from wings, after the vortex structures develop along the axis for a certain distance, the aerodynamic interference of wings weakens and the complex vortex structures dissipate gradually.

Figure 11 shows the definition of azimuth θ on a cross section plane along the axis. Pressure coefficients C_p distribution on different cutting planes of body (excluding the area of wings and tails) are shown in Figure 12, it can be seen that the C_p distributions on the windward side are similar to cosine distributions, while the C_p distributions on the leeward side is obviously affected by the asymmetric separation vortices. The C_p curve clearly reflects suction peaks caused by primary separation and secondary separation. Due to the asymmetric pressure distribution on the leeward side, it will induce side force along with roll and yaw moment. On the body between wings and fins, the cosine crest is flattened by the aerodynamic interference. Figure 13 shows the iteration history of lateral-directional force/moment coefficient, indicating that $C_S, C_{M,X}, C_{M,Z}$ of missile are relatively weak in this flight state, only roughly equivalent to the magnitude of C_A.

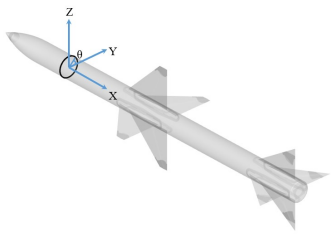

Figure 11 Definition of azimuth θ.

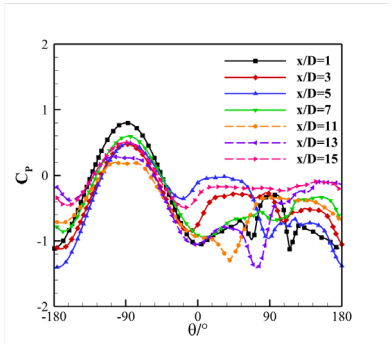

Figure 12 Pressure coefficient C_p distribution on different cross section planes.

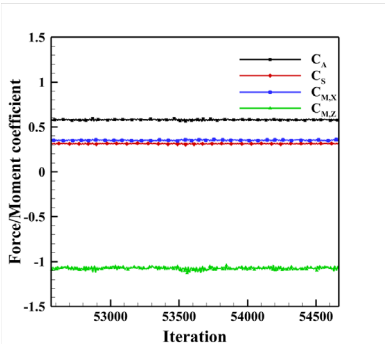

Figure 13 Iteration history of lateral-directional force/moment coefficient.

5. Conclusions

In this paper, a high-accurate numerical simulation of vortex-dominated flow over the Sparrow III type missile at high angles of attack is conducted by using a novel fifth-order WENO scheme and IDDES method.

(1) The results of RANS simulation indicate that using the high-order and low-dissipation WENO-K scheme to discretize inviscid flux can improve the computational accuracy of aerodynamic characteristic.

(2) The results of IDDES demonstrate that IDDES method has the ability to capture unsteady multi-scale vortices which are timely averaged by RANS method. The accurate numerical simulation method combing high-order scheme and IDDES method can give a good present for sophisticated vortex structure and interference of vortices between components.

(3) The generation, development, and evolution of vortical flow over missiles at high angles of attack is simulated and analyzed, and the mechanism of vortices interference is addressed. More detailed and in-depth research will be carried out in the future work.

6. Acknowledgement

This research was sponsored by the Science Fund for Distinguished Young Scholars of Shaanxi Province of China [grant No. 2020JC-13]. The work was carried out at National Supercomputer Center in Xi'an, and the calculations were performed on Sugon.

7. Contact Author Email Address

Wen-Ping Song*, Professor, wpsong@nwpu.edu.cn, corresponding author

8. Copyright Statement

References

[1] Allen H J, Perkins E W. A study of effects of viscosity on flow over slender inclined bodies of revolution[J]. Technical Report Archive & Image Library, 1951.

[2] ZILLIAC G G, DEGANI D, TOBAK M. Asymmetric Vortices on A Slender Body of Revolution[J]. AIAA Journal, 1991, 29(5): 667-675.

[3] XU Ke-zhe, ZHANG Yu-fei, CHEN Hai-xin, et al. Numerical study of nonlinear induced rolling moment of finned missile at high angle of attack[J]. Acta Aeronautica et Astronautica Sinica, 2014, 035(001):97-104.

[4] Zhang Li-feng, Li Dong. Numerical Simulation Study on Asymmetry Detached Flow of a Slender Body at High Angles of Attack[J]. Science Technology and Engineering, 2008, 008(008):2272-2275.

[5] Wang Fangjian, Wang Hongwei, Li Xiaohui, Dong Lei, Huang Zhan, Chen Lan. Subsonic unsteady aerodynamic characteristics on slender revolutionary body at extra-wide angle-of-attack. Chinese Journal of Theoretical and Applied Mechanics, 2022, 54(2): 379-395.

[6] Liu X D, Osher S, Chan T. Weighted Essentially Non-Oscillatory Schemes[J]. Journal of Computational Physics, 1994, 115(1):200-212.

[7] Jiang G, Shu C W. Efficient Implementation of Weighted ENO Schemes[J]. Journal of Computational Physics, 1996.

[8] Henrick A K, Aslam T D, Powers J M. Mapped weighted essentially non-oscillatory schemes: Achieving optimal order near critical points[M]. Academic Press Professional, Inc. 2005.

[9] Borges R, Carmona M, Costa B, et al. An improved weighted essentially non-oscillatory scheme for hyperbolic conservation laws[J]. Journal of Computational Physics, 2008, 227(6):3191-3211.

[10] Hu X Y, Wang Q, Adams N A. An adaptive central-upwind weighted essentially non-oscillatory scheme[J]. Journal of Computational Physics, 2010, 229(23): 8952-8965.

[11] Han S Q, Song W P, Han Z H. An Improved WENO Method based on Gauss-kriging Reconstruction with an Optimized Hyper-Parameter[J]. Journal of Computational Physics, 2020:109742.

[12] Han S Q, Song W P, Han Z H. A novel high-order scheme for numerical simulation of wake flow over helicopter rotors in hover, Chinese Journal of Aeronautics, 2021.

[13] Spalart P R. Strategies for turbulence modeling and simulations[J]. International Journal of Heat and Fluid Flow, 2000(21): 252-263.

[14] Spalart P R, Jou W H, Strelets M, et al. Comments on the feasibility of LES for wings, and on a hybrid RANS/LES approach[C]. Advances in DNS/LES. 1997.

[15] Young-person's guide to detached-eddy simulation grids[R]. NASA-TM-2001-211032.

[16] Shur M L, Spalart P R, Strelets M K, et al. A hybrid RANS-LES approach with delayed-DES and wall-modelled LES capabilities[J]. International Journal of Heat & Fluid Flow, 2008, 29(6):1638-1649.

[17] Spalart P R, Deck S, Shur M L, et al. A new version of detached-eddy simulation, resistant to ambiguous grid densities[J]. Theoretical & Computational Fluid Dynamics, 2006, 20(3):181.

[18] Abe K. A hybrid LES/RANS approach using an anisotropy-resolving algebraic turbulence model[J]. International Journal of Heat & Fluid Flow, 2005, 26(2):204-222.

[19] Spalart P R, Allmaras S R. A One-Equation Turbulence Model for Aerodynamic Flows. 1994.

[20] Shur M, Spalart P R, Strelets M, et al. Detached Eddy Simulation of an Airfoil at High Angle of Attack[J]. engineering turbulence modeling & experiments, 1999.

[21] Monta W J. Supersonic aerodynamic characteristics of a Sparrow 3 type missile model with wing controls and comparison with existing tail-control results. 1977.

[22] Swalwell K E, Sheridan J, Melbourne W H. Frequency Analysis of Surface Pressures on an Airfoil After Stall[C]// Aiaa, Applied Aerodynamics Conference. 2003.

[23] Haase W, Braza M, Revell A. DESider – A European Effort on Hybrid RANS-LES Modelling[J]. Springer, 2009, 103:341-346.

[24] Jian L, Sun H, Liu Z, et al. Numerical investigation of unsteady vortex breakdown past 80°/65° double-delta wing[J]. Chinese Journal of Aeronautics, 2014(3):10.

[25] John, E, Bernhardt, et al. Proportional Control of Asymmetric Forebody Vortices[J]. AIAA Journal, 1998, 36(11):2087-2087.